



# Post-annealing tailored 3D cross-linked $\text{TiNb}_2\text{O}_7$ nanorod electrode: towards superior lithium storage for flexible lithium-ion capacitors

Bohua Deng<sup>1</sup>, Haoyang Dong<sup>1</sup>, Tianyu Lei<sup>1</sup>, Ning Yue<sup>1</sup>, Liang Xiao<sup>1</sup> and Jinping Liu<sup>1,2\*</sup>

**ABSTRACT**  $\text{TiNb}_2\text{O}_7$  anode materials (TNO) have unique potential for applications in Li-ion capacitors (LICs) due to their high specific capacity of ca.  $280 \text{ mA h g}^{-1}$  over a wide anodic Li-insertion potential window. However, their high-rate capability is limited by their poor electronic and ionic conductivity. In particular, studies on TNO for LICs are lacking and that for flexible LICs have not yet been reported. Herein, a unique TNO porous electrode with cross-linked nanorods tailored by post-annealing and its application in flexible LICs are reported. This binder-free TNO anode exhibits superior rate performance ( $\sim 66.3\%$  capacity retention as the rate increases from 1 to 40 C), which is ascribed to the greatly shortened ion-diffusion length in TNO nanorods, facile electrolyte penetration and fast electron transport along the continuous single-crystalline nanorod network. Furthermore, the TNO anode shows an excellent cycling stability up to 2000 cycles and good flexibility (no capacity loss after continuous bending for 500 times). Model flexible LIC assembled with the TNO anode and activated carbon cathode exhibits increased gravimetric and volumetric energy/power densities ( $\sim 100.6 \text{ W h kg}^{-1}/4108.8 \text{ W kg}^{-1}$ ;  $10.7 \text{ mW h cm}^{-3}/419.3 \text{ mW cm}^{-3}$ ), more superior to previously reported hybrid supercapacitors. The device also efficiently powers an LED light upon  $180^\circ$  bending.

**Keywords:** post-annealing, cross-linked nanorods, facile electron transport, superior rate performance, flexible Li-ion capacitors

## INTRODUCTION

Li-ion capacitors (LICs) are hybrid energy-storage systems which are assembled with capacitive carbon electrodes and typical Li-ion battery electrodes [1–3]. They have attracted intensive research interest in the past two decades due to their merits such as increased energy

density and working voltage compared with supercapacitors (SCs) based on activated carbons, and much better cycling stability and rate capability compared with Li-ion batteries. Nevertheless, the high-rate capability and power density of LICs are limited by the sluggish electrochemical kinetics of electrode materials used in traditional Li-ion batteries [4–7]. To address this issue, electrode materials of batteries are usually prepared in nanoscale, which significantly improves their high-rate performance due to dramatically shortened Li-ion diffusion path in nanosized particles [4–9]. Recently, many efforts on LICs have been directed to the development of battery materials with specific nanostructures, especially high-potential anode materials [10–12]. It is well known that graphite anode may have the problem of Li metal deposition when discharged to about 0 V (vs.  $\text{Li/Li}^+$ ), which might lead to the combustion of organic electrolytes. The high-potential anode materials, mainly transition-metal oxides such as  $\text{Li}_4\text{Ti}_5\text{O}_{12}$  (LTO) and  $\text{Nb}_2\text{O}_5$  [13–36], can exhibit better safety performance at ultrahigh rates ( $> 10 \text{ C}$ ) compared with graphitized carbons. In this regard, advanced high-potential anode materials are very attractive for applications in LICs, especially when engineered to work at ultrahigh rates.

In the past decade,  $\text{TiNb}_2\text{O}_7$  (TNO) anode materials have been proposed for Li-ion batteries because of their considerably higher capacity compared with LTO and possibly lower cost after large-scale production [37–56]. TNO delivers a high reversible capacity of ca.  $280 \text{ mA h g}^{-1}$  (between 1.0 and 3.0 V), which is approximately twice that of LTO (ca.  $160 \text{ mA h g}^{-1}$ ) and close to that of commercial graphite (ca.  $300 \text{ mA h g}^{-1}$ ). Moreover, TNO can even store lithium at lower potential (down to 1.0 V; sloping charge/discharge profiles) com-

<sup>1</sup> School of Chemistry, Chemical Engineering and Life Sciences, Wuhan University of Technology, Wuhan 430070, China

<sup>2</sup> State Key Laboratory of Advanced Technology for Materials Synthesis and Processing, Wuhan University of Technology, Wuhan 430070, China

\* Corresponding author (email: [liujp@whut.edu.cn](mailto:liujp@whut.edu.cn))

pared with LTO (flat plateau at  $\sim 1.55$  V), enabling a wider anodic potential window which is quite promising for designing stable high-voltage LICs. Unfortunately, few studies have been reported on TNO materials for LICs [43,50–53]. In addition, TNO anodes generally have poor rate capability resulting from relatively low electronic and ionic conductivity. To improve the rate performance, previous efforts have been mainly devoted to nanostructured TNO materials with porous structure [44–50] or combined with conductive carbons [51–56]. While conductive agent is used to ensure the electrical conductivity, polymer binder is needed in the electrode preparation to guarantee physical/chemical connection between TNO particles. Moreover, the addition of electrochemically inactive binders increases the interfacial barriers for charge transfer and decreases the practical energy density [57]. Therefore, high-rate TNO anodes that are free of binder additive are more attractive for advanced LIC devices.

Recently, there is rapid development of bendable or wearable electronic devices such as roll-up displays, smart watches and flexible solar cells [58–61]. Therefore, researchers are increasingly motivated to develop flexible energy-storage systems compatible with such emerging electronics. Flexible energy storage devices require not only high energy and power densities, but also good mechanical properties to ensure robust flexibility or bendability. As a result, a promising design principle of using binder-free electrode-based hybrid capacitors was recently proposed by our group [15,62–63]. The direct growth of three-dimensional (3D) electrode architecture on flexible current collectors has been proven to fulfil all the electrochemical and mechanical requirements for advanced flexible LICs [64]. Despite this, flexible LICs based on TNO anode have not been reported until now.

Herein, an elaborate post-annealing tailored TNO porous anode with interconnected nanorods is prepared, which is used to construct TNO-based flexible LICs for the first time. As illustrated in Fig. 1, several advantages can be envisioned for our TNO anode: (i) dramatically reduced Li-ion diffusion path within the TNO nanorods ( $< 25$  nm); (ii) electrolyte accessibility ensuring facile Li-ion migration in porous nanostructure; (iii) fast electron transport along the cross-linked single-crystal TNO nanorods (reduced interfacial barriers due to absence of binder); (iv) enhanced nanostructure stability during cycling because of the cross-linking between TNO nanorods; and (v) good flexibility due to the direct growth of nanorod 3D framework on the flexible carbon cloth. Consequently, these TNO anodes exhibit superior rate

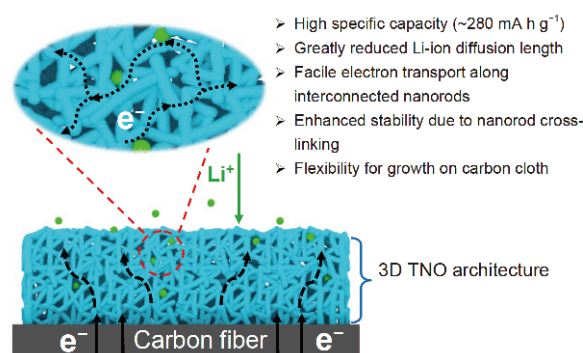


**Figure 1** Schematic illustration of the merits of TNO electrode architecture for Li-ion storage.

capability up to 40 C, excellent cycling stability of 2000 times and continuous bendability ( $> 500$  times). Model LICs constructed with the TNO anode and activated carbon cathode deliver increased energy/power densities and good cycling stability. The maximum gravimetric/volumetric energy densities were higher than those of other flexible SCs or battery-SC hybrid devices in previous literature. The present work provides an effective strategy to design high-performance flexible hybrid supercapacitors.

## EXPERIMENTAL SECTION

### Materials preparation

Firstly, seeded carbon cloths were prepared by immersing pristine carbon cloths in an ethanol solution with  $0.2 \text{ mol L}^{-1}$  niobium chloride ( $\text{NbCl}_5$ ) and  $0.1 \text{ mol L}^{-1}$  tetrabutyl titanate ( $\text{Ti}(\text{OC}_4\text{O}_9)_4$ ) for 24 h and then post-annealing at  $400^\circ\text{C}$  for 1 h. Secondly, a piece of seeded carbon cloth was placed in a Teflon-lined reactor (100 mL) containing a mixed solution, which was prepared by mixing 60 mL aqueous solution of HCl ( $6.6 \text{ mol L}^{-1}$ ) and 20 mL ethanol solution with  $0.2 \text{ mmol L}^{-1}$   $\text{NbCl}_5$  and  $0.1 \text{ mol L}^{-1}$   $\text{Ti}(\text{OC}_4\text{O}_9)_4$ . The Teflon-lined reactor was sealed with a stainless-steel autoclave, and then heated up and kept at  $200^\circ\text{C}$  for 24 h. After the solvothermal reaction, the carbon cloth was removed and then cleaned with distilled water and absolute alcohol successively. Thirdly, the as-prepared sample on the carbon cloth, as the precursor, was annealed under Ar atmosphere at different temperatures including 700, 750, 800 and  $850^\circ\text{C}$  for 5, 7, or 10 h. The mass-loading of TNO on the carbon cloth was estimated to be about  $2.0\text{--}2.5 \text{ mg cm}^{-2}$  by the comparison of pristine and final carbon cloths. All the chemicals used in this

work were analytical reagents and commercially supplied by Sinopharm Chemical Reagent Co. Ltd., China.

### Physical characterization

The morphologies of the TNO samples were examined by using scanning electron microscopy (SEM, Hitachi S-4800, Japan) and transmission electron microscopy (TEM, JEM-2010FEF, 200 kV), and the crystal structure was analyzed by using X-ray diffraction (XRD, Bruker D-8 Advance, Cu K $\alpha$ ). The surface chemistry of the as-prepared TNO was characterized by using X-ray photoelectron spectroscopy (XPS, Escalab 250-Xi, USA).

### Electrochemical measurements

The electrochemical performances of TNO anodes were tested in coin cells or soft packages which were assembled in an Ar-filled glove box. The electrolyte with 1 mol L<sup>-1</sup> LiPF<sub>6</sub> in ethylene carbonate (EC) and dimethyl carbonate (DMC) (in the volume ratio of 1:1), was commercially supplied by Guotai Huarong New Chemical Materials Co., China. In the half cells, Li metal was used as the counter electrode. In the LIC full cells, the as-prepared TNO and activated carbon (KYP-50, Kuraray) were used as the anode and cathode materials, respectively. The model flexible LICs in soft package were sealed with a polythene film.

Galvanostatic charge/discharge testing was conducted with a multi-channel battery testing system (Land-CT2001A, Wuhan Jinnuo, China). Cyclic voltammetry (CV) was performed with a CHI-660 electrochemical workstation (CH Instruments). Electrochemical impedance characterization was carried out on a PGSTAT100N electrochemical workstation (Autolab). The impedance spectra were recorded at the open circuit potential in the frequency range of 0.005 Hz to 1000 kHz with a potential amplitude of 10 mV. Before impedance examination, the half cells which were pre-charged for a preset capacity, were removed from the current load and then rested until the cell-potential variation was less than 5 mV in 1 h. The gravimetric or volumetric energy/power densities ( $E$  and  $P$ ) of the model LICs were calculated using  $E = \int_{t_1}^{t_2} IV(t)dt$  and  $P = E/\Delta t$ , where  $I$  is the constant current density (A g<sup>-1</sup> or A cm<sup>-3</sup>),  $V(t)$  is the working voltage at time  $t$ ,  $dt$  is time differential,  $t_1$  and  $t_2$  (s) are the start and end times of discharging, and  $\Delta t$  is the total discharging time. The mass used for calculation is based on the active electrode materials while the volume is based on all components including the current collector, anode, cathode, electrolyte and separator.

## RESULTS AND DISCUSSION

### Post-annealing tailored TNO anodes and Li-storage performances

The TNO anodes with tailored nanostructures were prepared by a facile solvothermal method and post-annealing under Ar atmosphere. The as-prepared electrodes are designated as TNO-700-5h, TNO-750-5h, TNO-800-5h, TNO-850-5h, TNO-750-7h and TNO-750-10h, respectively, highlighting the post-annealing temperature and time. Fig. 2a shows the surface morphologies of TNO-750-7h (with optimized annealing temperature and time). It can be seen that cross-linked short nanorods are uniformly decorated on the carbon fiber. The average diameter and length of the nanorods are estimated to be about ca. 25 and 80 nm, respectively. Moreover, nanopores are formed between cross-linked TNO nanorods. The cross-sectional image of TNO-750-7h is shown in Fig. 2b, which indicates the existence of a 3D porous (average pore diameter of ca. 6.431 nm and a

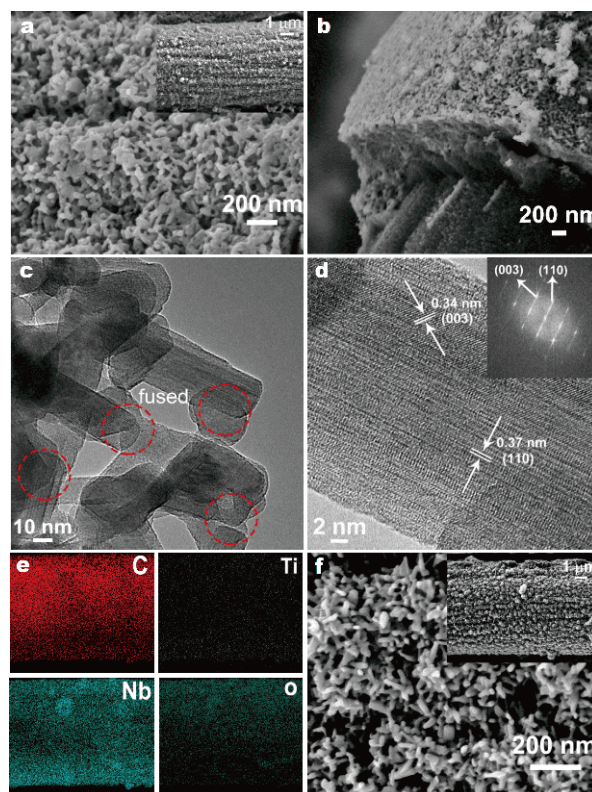


**Figure 2** (a) SEM images of TNO-750-7h (optimized). (b) Cross-sectional image of TNO-750-7h. (c, d) TEM images and SAED pattern of the nanorods from TNO-750-7h. (e) Energy dispersive spectrometer (EDS) elemental mapping images of TNO-750-7h. (f) SEM images of TNO-750-5h.



Brunauer-Emmett-Teller (BET) surface area of ca.  $39.652 \text{ m}^2 \text{ g}^{-1}$ , see Table S1) but integrated nanotexture (about  $1 \mu\text{m}$  in thickness). For further analysis, some TNO nanorods were mechanically scraped from TNO-750-7h and then characterized by TEM. As displayed in Fig. 2c, the cross-linking or fusion between well-crystallized nanorods also can be observed clearly (noted by red circles). In Fig. 2d, the lattice spacings of 0.34 and 0.37 nm are in good agreement with the (003) and (110) planes of  $C_2/m$  monoclinic TNO phase, respectively [37–49]. Moreover, the single-crystalline nature of TNO nanorods is evident from the selected area electron diffraction (SAED) pattern (inset in Fig. 2d), which would be beneficial to directing electron transfer within the nanotexture. The elemental mapping results of a single carbon fiber from TNO-750-7h are displayed in Fig. 2e. As expected, Ti, Nb and O elements are detected, confirming the formation of TNO nanorods.

The formation of the 3D porous nanotexture of TNO-750-7h can be attributed to the optimized post-annealing temperature and time. In contrast, almost no cross-linking between TNO nanorods is observed for TNO-750-5h (Fig. 2f) and other TNO materials (Fig. S1, Supplementary information) prepared with different annealing temperatures and times. For the precursor (after hydrothermal reaction but without post-annealing), a large number of tiny nanowhiskers are observed, which are uniformly distributed on the carbon fibers (Fig. S1a). After being annealed at high temperatures, the nanowhiskers are transformed into short nanorods (Fig. 2f and Fig. S1b, c). With elevated annealing temperatures from 700 to  $800^\circ\text{C}$ , increased average diameter (from 20 to 35 nm) but nearly unchanged average-length (ca. 80 nm) are observed for the TNO nanorods. Particularly, the short nanorods are observed to evolve into larger irregular nanoparticles after being annealed at  $800^\circ\text{C}$  (TNO-800-5h, Fig. S1c). Similarly, nanorods with increased average diameter (ca. 40 nm) and severe agglomeration are obtained after a ultra-long post-annealing time (TNO-750-10h, Fig. S1d).

The crystal structure and surface chemistry of TNO anodes were characterized by using XRD and XPS. Fig. 3a shows the XRD diffraction patterns of TNO samples prepared with different post-annealing temperatures. To better understand the structural phase of the TNO nanorods, the powder samples in the Teflon reactor were collected after hydrothermal reaction and then annealed at different temperatures. The diffraction patterns of the TNO powder samples were also examined, which are shown in Fig. 3b for comparison. Similar diffraction

patterns are observed for the powder samples with different annealing temperatures, which indicates that there is no change in the crystal phase. It is observed that these diffraction patterns are markedly different from those of  $\text{Nb}_2\text{O}_5$  powder samples [26–28], which indicates that TNO is formed instead of  $\text{Nb}_2\text{O}_5$ . By careful comparison with previous reported results, all the typical diffraction peaks are assigned to the monoclinic phase of  $C_2/m$  (PDF#77-1374) for TNO [37–49]. For the TNO samples grown on carbon cloth (Fig. 3a), the typical diffraction peaks of TNO are suppressed by the peaks of carbon fibers, especially for those with low post-annealing temperatures ( $< 800^\circ\text{C}$ ). Nevertheless, the main diffraction peaks are in good agreement with those of TNO powder samples. Furthermore, the formation of TNO on the carbon fibers is confirmed by the XPS results. The full XPS absorption and characteristic spectra of O 1s, Nb 3d and Ti 2p are displayed in Fig. 3c–f, respectively. The appearance of Nb 3d absorption peaks ( $3d_{3/2}$ ,  $3d_{5/2}$ ) at 210.5 and 207.7 eV, and Ti 2p peaks ( $2p_{1/2}$ ,  $2p_{3/2}$ ) at 464.7 and 459.6 eV indicates the presence of  $\text{Nb}^{5+}$  and  $\text{Ti}^{4+}$  in the oxide materials. In addition, the absorption intensity of C 1s, which originates from the carbon fibers under the TNO nanorods, is much lower than that of Nb 3d and O 1s (Fig. 3c). This implies that the carbon fibers are uniformly covered by the TNO nanorods. The above XRD and XPS results clearly confirm the successful growth of TNO anodes of crystallized monoclinic phase on the carbon cloth.

The electrochemical Li-storage performances of TNO materials with different annealing temperatures and times were examined by galvanostatic testing. The initial two cycles at 0.5 C are shown in Fig. 4a for comparison, from which similar charge and discharge profiles are observed. Typically, the charge/discharge process exhibits a flat plateau at ca. 1.7 V followed by a slope line (ca. 1.5–1.0 V), and a reversible capacity of ca.  $260 \text{ mA h g}^{-1}$  between 1.0 and 3.0 V. The rate performances of the TNO anodes were also tested, as shown in Fig. 4b. The electrodes show significantly improved rate capability compared with previously reported bulk materials [37–39], which can be ascribed mainly to the dramatically reduced Li-ion diffusion length within TNO nanorods. By comparison, TNO-750-5h and TNO-800-5h exhibit better rate performances than TNO-700-5h, especially at high rates above 10 C. This can be mainly ascribed to the better crystallization at elevated annealing temperature (Fig. 3a). Moreover, the high-rate performances of TNO-750-5h and TNO-800-5h are very similar ( $\sim 78.3\%$ ,  $70.5\%$ ,  $66.7\%$  and  $63.5\%$  of the reversible capacity at 1 C are

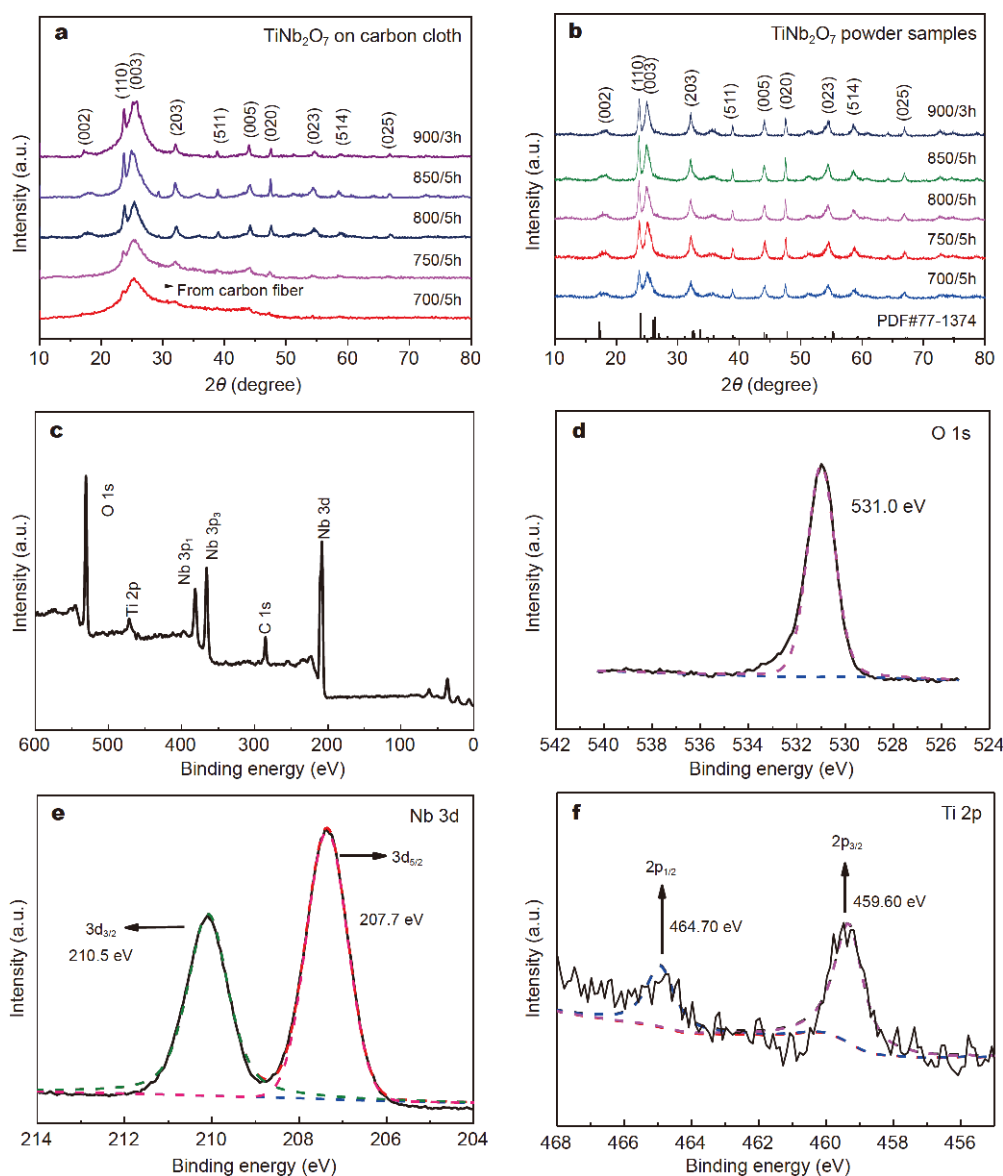


**Figure 3** (a) XRD patterns for TNO materials on the carbon cloth. (b) XRD patterns for TNO powder materials. (c–f) XPS spectra of TNO materials on the carbon cloth.

retained at 10, 20, 30 and 40 C, respectively). With optimized annealing time, TNO-750-7h exhibits further improved high-rate performance, and about 82.6%, 73.4% and 66.3% of 1 C capacity are retained at 10, 20 and 40 C, respectively. It is worth mentioning that such high-rate capability is encouraging for TNO electrodes with mass loading of 2.5–3.0 mg cm<sup>-2</sup> and no addition of conductive agent. This rate performance is comparable to the record high-level of TNO anode reported by Guo *et al.* (ca. 84.6%, 75% and 49% at 10, 20, and 50 C, respectively with mass loading of 1.5–2.0 mg cm<sup>-2</sup>) [44]. Fig. 4c shows the

typical charge/discharge profiles of TNO-750-7h at various C rates. Very high coulombic efficiency (~100%) and unchanged electrochemical characteristics are observed at various high rates (> 10 C). This improved high-rate performance of TNO-750-7h is ascribed to the facile electron transport along the 3D nanorod framework constructed with single-crystallized TNO nanorods. In contrast, inferior high-rate performances are observed for TNO-850-5h with higher crystallization degree and TNO-750-10h (Fig. S2c). This can be ascribed to the severe agglomeration of TNO nanorods after annealing at ultra-

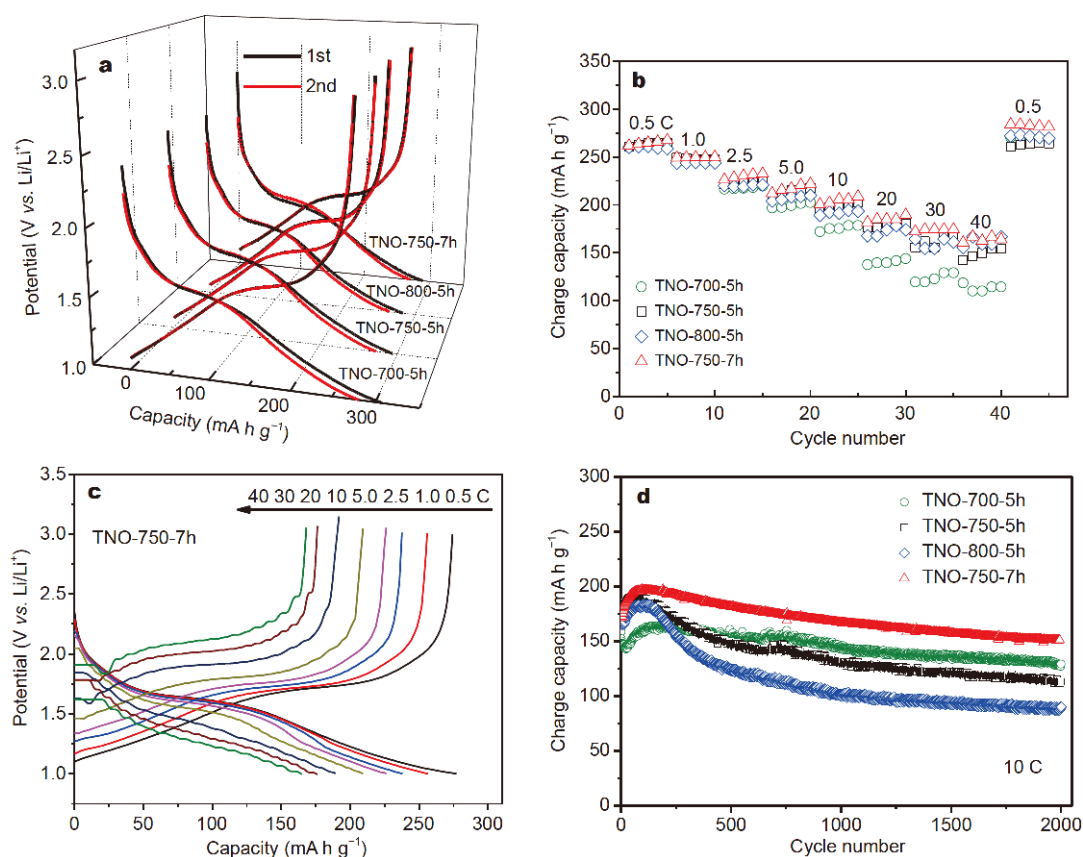


**Figure 4** Li-storage performances of TNO anodes. (a) The discharge/charge profiles at 0.5 C in the initial two cycles. (b) Rate performance of TNO anodes. (c) Typical discharge and charge curves of TNO-750-7h at various rates. (d) Cycling performance between 1.1 and 3.0 V at 10 C.

high temperature (TNO-850-5h) or with ultra-long time (TNO-750-10h), which likely leads to the poor contact of TNO nanorods with carbon fibers and consequently increased charge transfer resistance (Fig. S1d). Similarly, low coulombic efficiency is observed for TNO-850-5h in the initial cycle (ca. 83%) and subsequent cycles (Fig. S2a). In contrast, much higher coulombic efficiencies in the initial cycle (ca. 90%) and following cycles (100%) are obtained for TNO-700-5h, TNO-750-5h and TNO-800-5h (Fig. 4a).

Furthermore, different cycling performances were observed for TNO materials with different annealing temperatures and times. As shown in Fig. 4d, with elevated post-annealing temperature, decreased cycling stability is observed for the TNO anodes between 1.1 and 3.0 V. TNO-700-5h exhibits much better cycling stability, and the capacity retention reaches up to ~91% and 82% after 1000 and 2000 cycles, respectively. However, TNO-700-5h exhibits much poorer high-rate capability than TNO-750-5h and TNO-800-5h (Fig. 4b). Based on the overall consideration of these results, post-annealing at 750°C

was selected to prepare TNO anodes with both high-rate performance and long-cycling stability in this work. With optimized annealing time, TNO-750-7h shows significantly improved cycling stability compared with TNO-750-5h and TNO-700-5h, and achieves capacity retentions of ca. 95.8% and 86.4% after 1000 and 2000 cycles, respectively. This is mainly associated with the enhanced architecture stability upon cycling, due to the cross-linking between TNO nanorods and subsequent formation of a unique 3D porous nano-texture (which is more pronounced in TNO-750-7h compared with other TNO anodes, as revealed by the SEM and TEM results in Fig. 2). In contrast, TNO-750-10h with ultra-long annealing time shows much poorer cycling stability (Fig. S2d). This is ascribed to the poor adhesion of individual TNO nanorods with the underlying carbon fibers due to the deteriorated nanostructure integration and self-agglomeration of TNO nanorods (Fig. S1d). Increase in capacity in the initial cycles is observed for the TNO materials in Fig. 4d, which might be due to the activation of TNO particles post-annealed at high tem-

peratures ( $>600^{\circ}\text{C}$ ). Based on the comparative investigations of post-annealing temperature and time, post-treatment at  $750^{\circ}\text{C}$  for 7 h (TNO-750-7h) was determined to be the optimal condition for the TNO anode growth.

### Electrochemical kinetics investigation on the TNO anodes

To further understand the reasons for improved high-rate performance of TNO-750-7h, comparative analyses with CV and alternating current impedance were conducted for TNO-750-7h and TNO-700-5h anodes. The typical CV curves of TNO-750-7h at slow sweeping rates are shown in Fig. 5a, and the characteristics consistent with previous reports are observed [37–50]. Typically, three pairs of redox peaks were detected at about 1.9, 1.7 and 1.3 V between 3.0 to 1.0 V, which are assigned to the redox couples of  $\text{Ti}^{4+}/\text{Ti}^{3+}$ ,  $\text{Nb}^{5+}/\text{Nb}^{4+}$  and  $\text{Nb}^{4+}/\text{Nb}^{3+}$ , respectively. The CV profiles of TNO-750-7h at different sweeping rates are displayed in Fig. 5b. It can be seen that the peak potential offset is small at sweeping rates below  $2.0\text{ mV s}^{-1}$ , and it increases significantly at sweeping rates above  $5.0\text{ mV s}^{-1}$ . These characteristics are also observed with TNO-700-5h (Fig. S3a). According to classic elec-

trochemical kinetics [65], a linear dependence of peak current ( $I_p$ ) on the square root of sweeping rates ( $v^{1/2}$ ) indicates a diffusion-controlled process. In contrast, the linear dependence of  $I_p$  on  $v$  shows the dominance of a surface process. To understand the Li-ion intercalation/extraction kinetics of the TNO anodes, the biggest peak at ca. 1.7 V corresponding to the main capacity of Li-storage, was selected for analysis. The cathodic and anodic  $I_p$  values at 1.7 V are plotted with  $v$  or  $v^{1/2}$ , respectively. As shown in Fig. 5c, d, the plotted points of both TNO-750-7h and TNO-700-5h are well fitted with a linear dependence of  $I_p$  on  $v^{1/2}$  at all sweeping rates. In contrast, only the data below  $2.0\text{ mV s}^{-1}$  are fitted with a linear relationship of  $I_p$  with  $v$ . The CV analysis results indicate that the rate performance of the TNO anodes is limited by Li-ion diffusion within TNO, especially at high rates. Accordingly, the TNO nanorod anodes exhibit significantly improved rate performance compared with bulk counterparts in large crystal size, due to the dramatically reduced Li-ion diffusion path in the nanorods.

It is well understood that the high-rate capability of Li-ion intercalation materials is affected not only by the Li-

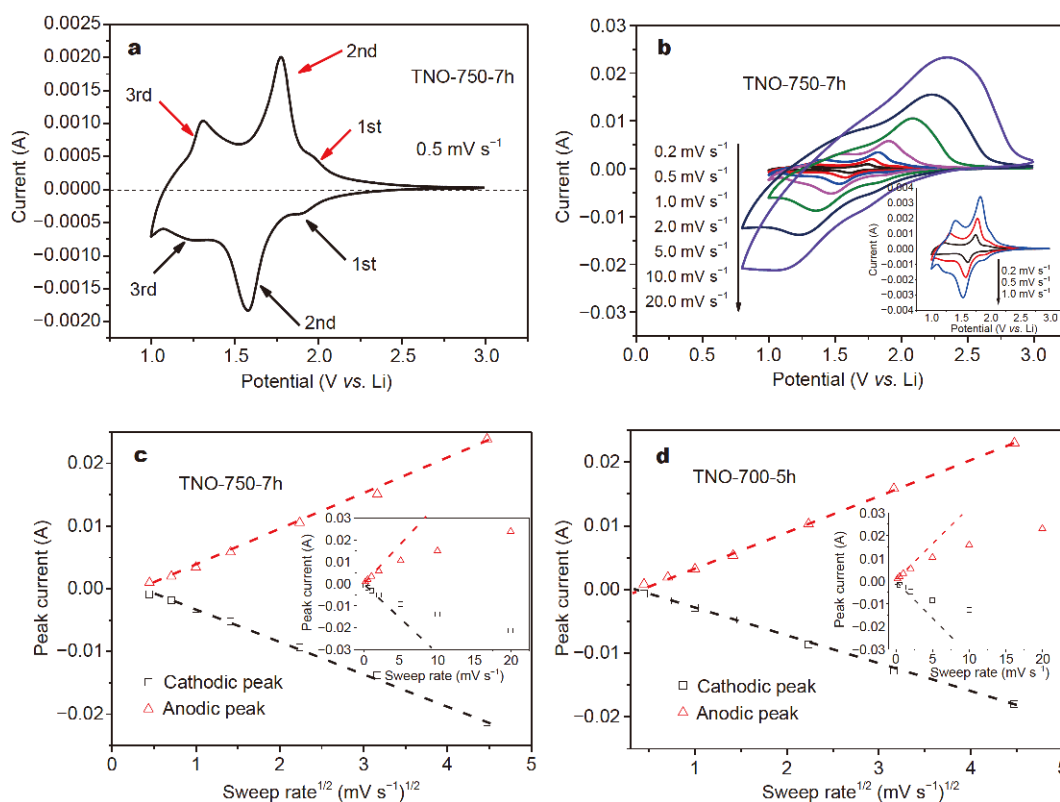


**Figure 5** (a, b) CV profiles of TNO-750-7h at various sweeping rates. (c, d) Plots of the peak current with sweeping rates for TNO-750-7h and TNO-700-5h.

ion diffusion in solid phase, but also by the interfacial charge transfer. The impedances of TNO-750-7h and TNO-700-5h anodes were thus characterized for better understanding the improved high-rate performances. The Nyquist plots for the measured impedance spectra of TNO-750-7h are presented in Fig. 6a in scattered dots. All the spectra measured at charged states (below 2.30 V) exhibit a depressed large semicircle in the high frequency range, a small semicircle in the middle frequency range and a sloping line in the low frequency region. Similar characteristics are also observed for TNO-700-5h (Fig. S3b). According to previous research [66–68], the first semicircle which does not change with the discharged capacity, is associated with the Li-ion migration through the passive film on the material surface. The second semicircle which varies with the discharged capacity, is assigned to the charge transfer process. The sloping lines in the low frequency region are attributed to the Li-ion diffusion in the TNO nanorods. In addition, the sloping grades were observed to be much larger than

45° for a semi-infinite diffusion. This can be ascribed to the proceeding of a finite diffusion, in accordance with the limited diffusion length within the TNO nanorods.

The impedance spectra in Fig. 6a were further analyzed with a modified Randles equivalent circuit (inset of Fig. 6b). In the circuit, two  $R||CPEs$  ( $R$ , resistance;  $CPE$ , constant phase element) in series were introduced to simulate the depressed semicircle in high frequency region, which corresponds to the surface film. The charge transfer resistance ( $R_{ct}$ ) in parallel with a  $CPE$  was used to simulate the second semicircle associated with the charge transfer process. In addition, a finite-length Warburg impedance ( $Z_{ws}$ ) in series with a pseudocapacitance ( $C_\phi$ ) was introduced to fit the sloping lines corresponding to the finite diffusion of Li-ions in the TNO nanorods [67–69]. With the modified equivalent circuit, the Zview software was used to fit the measured impedance data, and the fitted results in Nyquist plots are also displayed in Fig. 6a (in solid lines). It can be seen that the measured impedance spectra in scattered dots are well fitted by the

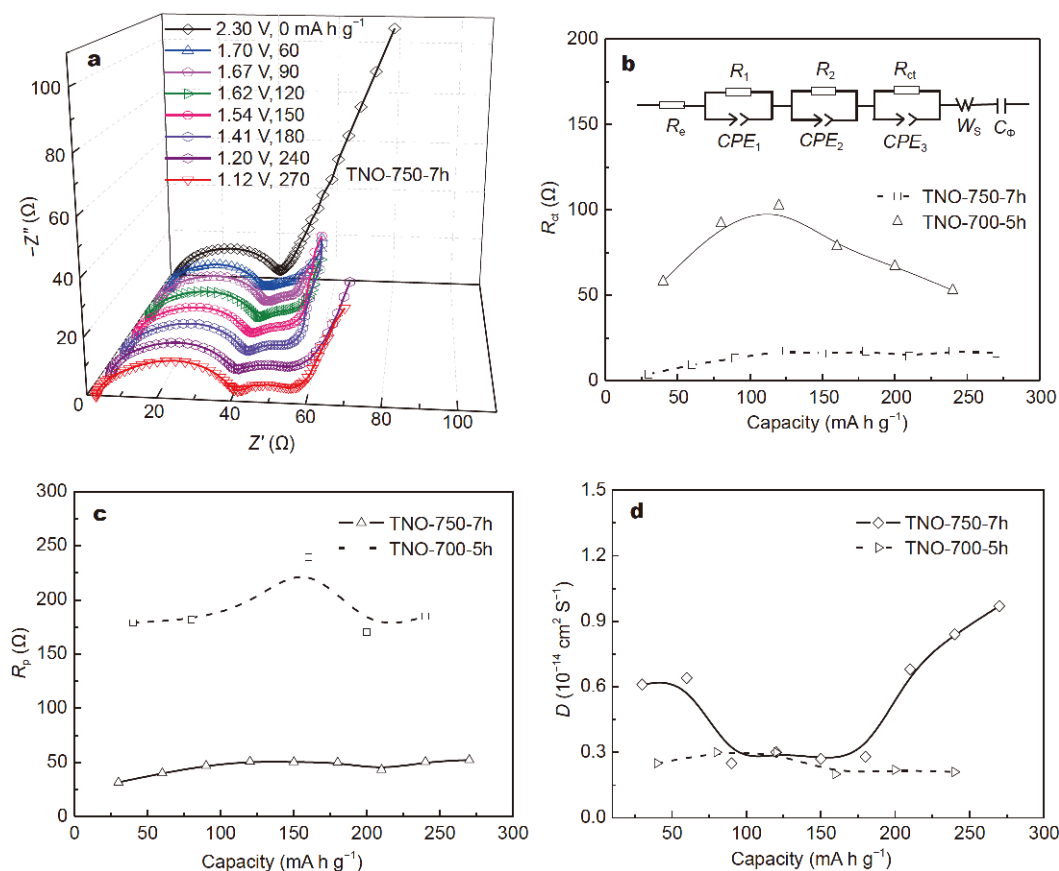


**Figure 6** (a) Nyquist plots for the impedance data of TNO-750-7h at different charged states (experimental and fitted data in dots and solid lines, respectively). (b–d) Plots of  $R_{ct}$ ,  $R_p$  and  $D_{Li^+}$  with the discharge capacity for TNO-750-7h and TNO-700-5h.



modified equivalent circuit. Similar result was also observed for TNO-700-5h anode (Fig. S3b). The values of  $R_{ct}$ ,  $R_p$  (the polarization resistance, including the resistances of surface film and charge transfer) and the Li-ion diffusion coefficient ( $D_{Li^+}$ ) obtained by the fitted data, were plotted against the discharge capacity, as shown in Fig. 6b–d. Compared with TNO-700-5h, significantly reduced  $R_{ct}$  and  $R_p$  values for TNO-750-7h are observed in Fig. 6b, c. It has been widely verified that reduced  $R_{ct}$  and  $R_p$ , which are helpful to improve the charging rate, are achieved by improved crystallization of intercalation materials. This general reason could be applicable to the TNO-750-7h anode as well. Moreover, the  $R_{ct}$  of TNO-750-7h are further reduced by the enhanced electron transfer along the cross-linked single-crystal nanorods. It is likely that the facile Li-ion migration within the porous but continuous film architecture of TNO-750-7h contributes partly to the reduced  $R_p$ .

The  $D_{Li^+}$  was calculated approximately by using the parameter  $T$  for the  $Z_{ws}$ . The data of  $T$  are obtained with the following equation by setting  $P = 0.5$  [69],

$$Z_{ws} = R_D(j\omega T)^{-P} \tanh([j\omega T]^P), \quad (1)$$

where  $R_D$  represents the low-frequency limit of  $Z_{ws}$  (the Warburg impedance of finite-length diffusion),  $j = \sqrt{-1}$ ,  $\omega$  is the angular frequency,  $T = l^2/D$  and  $P$  represents varying exponent (01). Then, the chemical diffusion coefficient ( $D$ ) was calculated by using  $T = l^2/D$ , where  $l$  represents the diffusion length. The value of  $l$  was estimated by the half diameter of TNO nanorods. The calculated  $D_{Li^+}$  values of both TNO-700-5h and TNO-750-7h are found to vary in the order of  $10^{-15}$ – $10^{-14}$   $\text{cm}^2 \text{s}^{-1}$  (Fig. 6d). Moreover, the  $D_{Li^+}$  value of TNO-750-7h is slightly larger than that of TNO-700-5h, which can also be attributed to the elevated temperature-induced better crystallization that may enable facile Li-ion diffusion in the nanorods.

Based on the above analysis, it can be concluded that the Li storage process in TNO anodes is diffusion-controlled. Nevertheless, after optimization of the post-annealing temperature and time, significantly reduced  $R_{ct}$ ,  $R_p$  and  $l$  as well as improved  $D_{Li^+}$  are achieved with the designed 3D interconnected nanorod electrode architecture.

#### Electrochemical performance of LIC based on TNO-750-7h

To further demonstrate the advantages of TNO-750-7h with unique nanotexture, a model LIC with TNO-750-7h anode and activated carbon (AC) cathode was assembled and tested. The galvanostatic charge/discharge behaviors

of commercial AC (KYP-50) cathode were first examined (Fig. S4). Sloped straight lines corresponding to a capacitive behavior between 3.0 and 4.5 V (vs.  $\text{Li}^+/\text{Li}$ ), and a reversible capacity of ca.  $50 \text{ mA h g}^{-1}$  at 2 C are observed (Fig. S4a). The KYP-50 cathode exhibits excellent high-rate capability, with ~90%, 84% and 73% of the discharge capacity at 2 C being retained at 10, 20 and 40 C, respectively (Fig. S4b). Moreover, it shows superior cycling stability as displayed in Fig. S4c (capacity retentions of ca. 97.1% and 96.4% after 1000 and 2000 cycles, respectively).

The electrochemical performances of the assembled LIC are shown in Fig. 7. To obtain high energy and power densities, the mass ratio of TNO to KYP-50 was optimized to be 1:4.2. Fig. 7a displays the typical charge/discharge profiles of the model LIC in coin cell between 1.0 and 3.5 V. Different from the sloping straight lines for KYP-50, inclined charge/discharge curves are observed for the LIC because of the combination of battery-type TNO anode and capacitive AC cathode. The optimized LIC device delivers a reversible capacity of ca.  $43 \text{ mA h g}^{-1}$  at 2 C. It also exhibits superior high-rate capability. As shown in Fig. 7b, capacity retention of ~84%, 77%, 60% and 54% are reached when the rate increases from 2 to 10, 20, 30 and 40 C, respectively. In addition, a capacity retention of ca. 88% is obtained after 1000 cycles at 10 C for the device (Fig. 7c), indicative of good cycling performance.

Different from other nanostructured TNO anodes in previous reports [44–56], the TNO anode in this work also exhibits good flexibility, which benefits from the direct growth of a 3D TNO nanorod film on flexible carbon cloth. To demonstrate its flexibility, the TNO-750-7h anode was bent repeatedly for 500 times (inset of Fig. 7d; optical images before and after the bending), and then an LIC device assembled with the bending-treated TNO-750-7h was tested. No TNO film peel-off is observed after continuous bending, and there is almost no change in the charge/discharge curves of LIC device (Fig. 7d). In addition, a flexible LIC in soft package was assembled with TNO-750-7h and KYP-50, which is able to light up a white LED indicator even when bent from 0 to 180° (inset of Fig. 7c).

Furthermore, the new LIC device exhibits increased energy and power densities. The Ragone plot for the gravimetric energy density versus power density of the device is illustrated in Fig. 7e, along with the data of previously reported LICs for comparison [70–75]. The as-prepared LIC delivers a higher gravimetric energy density at the similar power density compared with previously reported LICs based on titanium/niobium/vanadium-

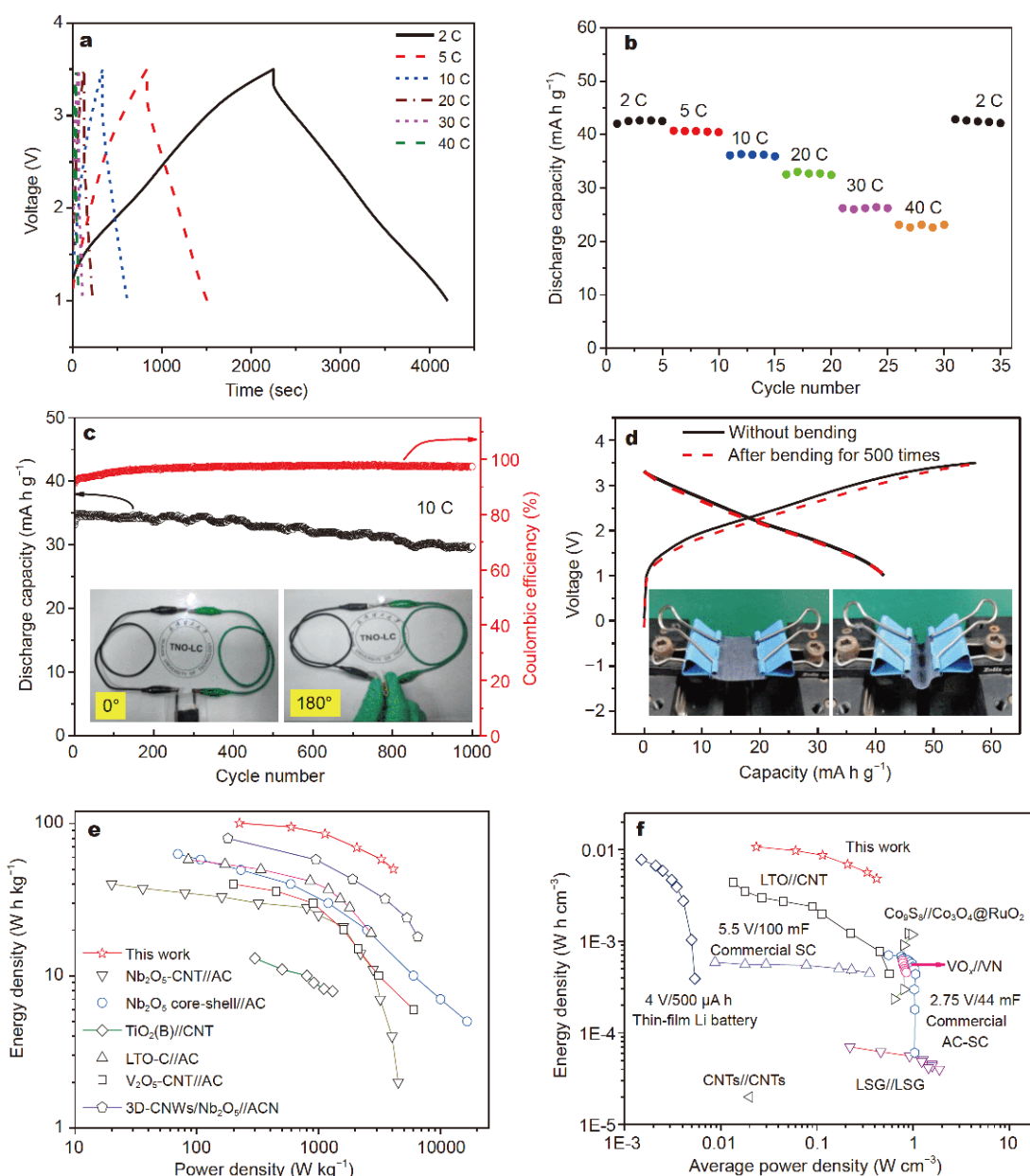


**Figure 7** (a) Typical charge/discharge profiles for the model LIC at various rates. (b) Rate performance of the model LIC. (c) Cycling performance of the model LIC at 10 C. Insets show the optical images of a while LED indicator lit up by the LIC. (d) Charge/discharge profiles for the model LIC based on TNO-750-7h with or without continuous bending. Insets show continuous bending of TNO-750-7h. (e) Ragone plot of gravimetric energy density *versus* power density. (f) Ragone plot of volumetric energy density *versus* power density. Some previously reported data are also included for comparison.

oxide anodes. A maximum gravimetric energy density of ca.  $100.6 \text{ W h kg}^{-1}$  (at  $233.5 \text{ W kg}^{-1}$ ) is achieved, which is much larger than that of  $\text{Nb}_2\text{O}_5$  core-cell//AC ( $63 \text{ W h kg}^{-1}$  at  $70 \text{ W kg}^{-1}$ ) [72], 3D-CNWs/ $\text{Nb}_2\text{O}_5$ //ACN ( $79 \text{ W h kg}^{-1}$  at  $177 \text{ W kg}^{-1}$ ) [73], and LTO-C//AC ( $58 \text{ W h kg}^{-1}$  at  $85 \text{ W kg}^{-1}$ ) [75]. At a high power density of  $4108.8 \text{ W kg}^{-1}$ , the energy density is still as high as

$51 \text{ W h kg}^{-1}$ . In addition, the volumetric energy and power densities of the flexible LIC device are presented in Fig. 7f. For comparison, the data of some commercially available or previously reported flexible energy-storage devices are also summarized [15,76–80]. It is worth noting that the novel LIC exhibits a maximum volumetric energy density of ca.  $10.7 \text{ mW h cm}^{-3}$ , close to that of the

commercial thin-film lithium battery [76] and much higher than that of other flexible LICs such as LTO//CNT ( $4.5 \text{ mW h cm}^{-3}$ ) [15] at a comparable power density [77–80]. Moreover, the highest volumetric power density of the novel device approaches that of the commercial AC SCs and  $5.5 \text{ V/100 mF SC}$ . The superior energy and power densities of this LIC are attributed to the 3D binder-free interconnected nanorod architecture of TNO, which enables greatly reduced Li-ion diffusion length and rapid ion diffusion as well as facile interfacial charge transfer.

## CONCLUSIONS

In summary, a flexible TNO anode with an integrated 3D nanotexture of cross-linked nanorods on carbon cloth was successfully prepared by a convenient solvothermal process and optimized post-annealing treatment. Benefitting from the absence of binder, good connections among individual nanorods and highly porous structure resulting from the cross-linked architecture, the TNO anode exhibits superior rate capability up to 40 C, excellent cycling stability (2000 times) and robust flexibility (no capacity loss after continuous bending for 500 times). Using the TNO anode and commercial AC cathode, a prototype LIC device was assembled, which delivers much higher gravimetric and volumetric energy/power densities compared with previous LICs based on titanium/niobium/vanadium-oxide anodes. Our work presents a promising strategy to develop high-rate and high-capacity battery electrodes for flexible LICs.

Received 14 October 2019; accepted 1 December 2019;  
published online 30 December 2019

- Amatucci GG, Badway F, Du Pasquier A, *et al.* An asymmetric hybrid nonaqueous energy storage cell. *J Electrochem Soc*, 2001, 148: A930
- Jiang Y, Liu J. Definitions of pseudocapacitive materials: a brief review. *Energy Environ Mater*, 2019, 2: 30–37
- Jabeen N, Hussain A, Xia Q, *et al.* High-performance 2.6 V aqueous asymmetric supercapacitors based on *in situ* formed  $\text{Na}_{0.5}\text{MnO}_2$  nanosheet assembled nanowall arrays. *Adv Mater*, 2017, 29: 1700804
- Naoi K, Ishimoto S, Miyamoto J, *et al.* Second generation ‘nano-hybrid supercapacitor’: evolution of capacitive energy storage devices. *Energy Environ Sci*, 2012, 5: 9363–9373
- Simon P, Gogotsi Y, Dunn B. Where do batteries end and supercapacitors begin? *Science*, 2014, 343: 1210–1211
- Wang H, Zhu C, Chao D, *et al.* Nonaqueous hybrid lithium-ion and sodium-ion capacitors. *Adv Mater*, 2017, 29: 1702093
- Zhang Y, Zhang Z, Tang Y, *et al.*  $\text{LiFePO}_4$  particles embedded in fast bifunctional conductor  $\text{rGO}\&\text{C@Li}_3\text{V}_2(\text{PO}_4)_3$  nanosheets as cathodes for high-performance Li-ion hybrid capacitors. *Adv Funct Mater*, 2019, 29: 1807895
- Aricò AS, Bruce P, Scrosati B, *et al.* Nanostructured materials for advanced energy conversion and storage devices. *Nat Mater*, 2005, 4: 366–377
- Augustyn V, Simon P, Dunn B. Pseudocapacitive oxide materials for high-rate electrochemical energy storage. *Energy Environ Sci*, 2014, 7: 1597–1614
- Aravindan V, Gnanaraj J, Lee YS, *et al.* Insertion-type electrodes for nonaqueous Li-ion capacitors. *Chem Rev*, 2014, 114: 11619–11635
- Ni J, Fu S, Wu C, *et al.* Superior sodium storage in  $\text{Na}_2\text{Ti}_3\text{O}_7$  nanotube arrays through surface engineering. *Adv Energy Mater*, 2016, 6: 1502568
- Gao X, Liu X, Wu D, *et al.* Significant role of Al in ternary layered double hydroxides for enhancing electrochemical performance of flexible asymmetric supercapacitor. *Adv Funct Mater*, 2019, 29: 1903879
- Ohzuku T. Zero-strain insertion material of  $\text{Li}[\text{Li}_{1/3}\text{Ti}_{5/3}]\text{O}_4$  for rechargeable lithium cells. *J Electrochem Soc*, 1995, 142: 1431–1435
- Naoi K, Ishimoto S, Isobe Y, *et al.* High-rate nano-crystalline  $\text{Li}_4\text{Ti}_5\text{O}_{12}$  attached on carbon nano-fibers for hybrid supercapacitors. *J Power Sources*, 2010, 195: 6250–6254
- Zuo W, Wang C, Li Y, *et al.* Directly grown nanostructured electrodes for high volumetric energy density binder-free hybrid supercapacitors: a case study of  $\text{CNTs/Li}_4\text{Ti}_5\text{O}_{12}$ . *Sci Rep*, 2015, 5: 7780–7788
- Zukalová M, Kalbác M, Kavan L, *et al.* Pseudocapacitive lithium storage in  $\text{TiO}_2$  (B). *Chem Mater*, 2005, 17: 1248–1255
- Liu S, Jia H, Han L, *et al.* Nanosheet-constructed porous  $\text{TiO}_2$ -B for advanced lithium ion batteries. *Adv Mater*, 2012, 24: 3201–3204
- Dylla AG, Henkelman G, Stevenson KJ. Lithium insertion in nanostructured  $\text{TiO}_2$  (B) architectures. *Acc Chem Res*, 2013, 46: 1104–1112
- Kim HS, Cook JB, Lin H, *et al.* Oxygen vacancies enhance pseudocapacitive charge storage properties of  $\text{MoO}_{3-x}$ . *Nat Mater*, 2017, 16: 454–460
- Cook JB, Kim HS, Lin TC, *et al.* Pseudocapacitive charge storage in thick composite  $\text{MoS}_2$  nanocrystal-based electrodes. *Adv Energy Mater*, 2017, 7: 1601283
- Li J, Tang Z, Zhang Z. Layered hydrogen titanate nanowires with novel lithium intercalation properties. *Chem Mater*, 2005, 17: 5848–5855
- Wang Y, Hong Z, Wei M, *et al.* Layered  $\text{H}_2\text{Ti}_6\text{O}_{13}$ -nanowires: A new promising pseudocapacitive material in non-aqueous electrolyte. *Adv Funct Mater*, 2012, 22: 5185–5193
- Cho W, Kashiwagi T, Ra W, *et al.* Relationship between electrochemical behavior and Li/vacancy arrangement in ramsdellite type  $\text{Li}_{2+x}\text{Ti}_3\text{O}_7$ . *Electrochim Acta*, 2009, 54: 1842–1850
- Chernova NA, Roppolo M, Dillon AC, *et al.* Layered vanadium and molybdenum oxides: batteries and electrochromics. *J Mater Chem*, 2009, 19: 2526–2552
- Li Q, Wei Q, Wang Q, *et al.* Self-template synthesis of hollow shell-controlled  $\text{Li}_3\text{VO}_4$  as a high-performance anode for lithium-ion batteries. *J Mater Chem A*, 2015, 3: 18839–18842
- Kumagai N. Thermodynamics and kinetics of lithium intercalation into  $\text{Nb}_2\text{O}_5$  electrodes for a 2 V rechargeable lithium battery. *J Electrochem Soc*, 1999, 146: 3203–3210
- Kim JW, Augustyn V, Dunn B. The effect of crystallinity on the rapid pseudocapacitive response of  $\text{Nb}_2\text{O}_5$ . *Adv Energy Mater*, 2011, 1: 100–104

- 2012, 2: 141–148
- 28 Augustyn V, Come J, Lowe MA, *et al.* High-rate electrochemical energy storage through  $\text{Li}^+$  intercalation pseudocapacitance. *Nat Mater*, 2013, 12: 518–522
  - 29 Wang H, Zhang Y, Ang H, *et al.* A high-energy lithium-ion capacitor by integration of a 3D interconnected titanium carbide nanoparticle chain anode with a pyridine-derived porous nitrogen-doped carbon cathode. *Adv Funct Mater*, 2016, 26: 3082–3093
  - 30 Sun YG, Sun TQ, Lin XJ, *et al.* Facile synthesis of hollow  $\text{Ti}_2\text{Nb}_{10}\text{O}_{29}$  microspheres for high-rate anode of Li-ion batteries. *Sci China Chem*, 2018, 61: 670–676
  - 31 Cai Y, Ku L, Wang L, *et al.* Engineering oxygen vacancies in hierarchically Li-rich layered oxide porous microspheres for high-rate lithium ion battery cathode. *Sci China Mater*, 2019, 62: 1374–1384
  - 32 Chen L, Jiang H, Hu Y, *et al.* In-situ growth of ultrathin  $\text{MoS}_2$  nanosheets on sponge-like carbon nanospheres for lithium-ion batteries. *Sci China Mater*, 2018, 61: 1049–1056
  - 33 Lou L, Kong X, Zhu T, *et al.* Facile fabrication of interconnected-mesoporous  $\text{T-Nb}_2\text{O}_5$  nanofibers as anodes for lithium-ion batteries. *Sci China Mater*, 2019, 62: 465–473
  - 34 Wu Y, Cao C. The way to improve the energy density of supercapacitors: Progress and perspective. *Sci China Mater*, 2018, 61: 1517–1526
  - 35 Huang ZD, Zhang TT, Lu H, *et al.* Bimetal-organic-framework derived  $\text{CoTiO}_3$  mesoporous micro-prisms anode for superior stable power sodium ion batteries. *Sci China Mater*, 2018, 61: 1057–1066
  - 36 Hou Y, Chang K, Wang Z, *et al.* Rapid microwave-assisted refluxing synthesis of hierarchical mulberry-shaped  $\text{Na}_3\text{V}_2(\text{PO}_4)_2\text{O}_2\text{F}$  @C as high performance cathode for sodium & lithium-ion batteries. *Sci China Mater*, 2019, 62: 474–486
  - 37 Han JT, Huang YH, Goodenough JB. New anode framework for rechargeable lithium batteries. *Chem Mater*, 2011, 23: 2027–2029
  - 38 Han JT, Goodenough JB. 3-V full cell performance of anode framework  $\text{TiNb}_2\text{O}_7$ /spinel  $\text{LiNi}_{0.5}\text{Mn}_{1.5}\text{O}_4$ . *Chem Mater*, 2011, 23: 3404–3407
  - 39 Lu X, Jian Z, Fang Z, *et al.* Atomic-scale investigation on lithium storage mechanism in  $\text{TiNb}_2\text{O}_7$ . *Energy Environ Sci*, 2011, 4: 2638–2644
  - 40 Tang K, Mu X, van Aken PA, *et al.* “Nano-pearl-string”  $\text{TiNb}_2\text{O}_7$  as anodes for rechargeable lithium batteries. *Adv Energy Mater*, 2013, 3: 49–53
  - 41 Takami N, Ise K, Harada Y, *et al.* High-energy, fast-charging, long-life lithium-ion batteries using  $\text{TiNb}_2\text{O}_7$  anodes for automotive applications. *J Power Sources*, 2018, 396: 429–436
  - 42 Deng Q, Fu Y, Zhu C, *et al.* Niobium-based oxides toward advanced electrochemical energy storage: recent advances and challenges. *Small*, 2019, 15: 1804884
  - 43 Aravindan V, Sundaramurthy J, Jain A, *et al.* Unveiling  $\text{TiNb}_2\text{O}_7$  as an insertion anode for lithium ion capacitors with high energy and power density. *ChemSusChem*, 2014, 7: 1858–1863
  - 44 Guo B, Yu X, Sun XG, *et al.* A long-life lithium-ion battery with a highly porous  $\text{TiNb}_2\text{O}_7$  anode for large-scale electrical energy storage. *Energy Environ Sci*, 2014, 7: 2220–2226
  - 45 Park H, Wu HB, Song T, *et al.* Porosity-controlled  $\text{TiNb}_2\text{O}_7$  microspheres with partial nitridation as a practical negative electrode for high-power lithium-ion batteries. *Adv Energy Mater*, 2015, 5: 1401945
  - 46 Park H, Shin DH, Song T, *et al.* Synthesis of hierarchical porous  $\text{TiNb}_2\text{O}_7$  nanotubes with controllable porosity and their application in high power Li-ion batteries. *J Mater Chem A*, 2017, 5: 6958–6965
  - 47 Jo C, Kim Y, Hwang J, *et al.* Block copolymer directed ordered mesostructured  $\text{TiNb}_2\text{O}_7$  multimetallic oxide constructed of nanocrystals as high power Li-ion battery anodes. *Chem Mater*, 2014, 26: 3508–3514
  - 48 Lou S, Cheng X, Zhao Y, *et al.* Superior performance of ordered macroporous  $\text{TiNb}_2\text{O}_7$  anodes for lithium ion batteries: Understanding from the structural and pseudocapacitive insights on achieving high rate capability. *Nano Energy*, 2017, 34: 15–25
  - 49 Liu G, Zhao L, Sun R, *et al.* Mesoporous  $\text{TiNb}_2\text{O}_7$  microspheres as high performance anode materials for lithium-ion batteries with high-rate capability and long cycle-life. *Electrochim Acta*, 2018, 259: 20–27
  - 50 Li H, Shen L, Wang J, *et al.* Three-dimensionally ordered porous  $\text{TiNb}_2\text{O}_7$  nanotubes: a superior anode material for next generation hybrid supercapacitors. *J Mater Chem A*, 2015, 3: 16785–16790
  - 51 Wang X, Shen G. Intercalation pseudo-capacitive  $\text{TiNb}_2\text{O}_7$ @carbon electrode for high-performance lithium ion hybrid electrochemical supercapacitors with ultrahigh energy density. *Nano Energy*, 2015, 15: 104–115
  - 52 Noh H, Choi W. Preparation of a  $\text{TiNb}_2\text{O}_7$  microsphere using formic acid and wrapping with reduced graphene oxide for anodes in lithium ion batteries. *J Electrochem Soc*, 2016, 163: A1042–A1049
  - 53 Jiao X, Hao Q, Xia X, *et al.* Boosting long-cycle-life energy storage with holey graphene supported  $\text{TiNb}_2\text{O}_7$  network nanostructure for lithium ion hybrid supercapacitors. *J Power Sources*, 2018, 403: 66–75
  - 54 Li S, Cao X, Schmidt CN, *et al.*  $\text{TiNb}_2\text{O}_7$ /graphene composites as high-rate anode materials for lithium/sodium ion batteries. *J Mater Chem A*, 2016, 4: 4242–4251
  - 55 Zhu G, Li Q, Zhao Y, *et al.* Nanoporous  $\text{TiNb}_2\text{O}_7$ /C composite microspheres with three-dimensional conductive network for long-cycle-life and high-rate-capability anode materials for lithium-ion batteries. *ACS Appl Mater Interfaces*, 2017, 9: 41258–41264
  - 56 Lin C, Hu L, Cheng C, *et al.* Nano- $\text{TiNb}_2\text{O}_7$ /carbon nanotubes composite anode for enhanced lithium-ion storage. *Electrochim Acta*, 2018, 260: 65–72
  - 57 Jiang J, Li Y, Liu J, *et al.* Recent advances in metal oxide-based electrode architecture design for electrochemical energy storage. *Adv Mater*, 2012, 24: 5166–5180
  - 58 Gwon H, Hong J, Kim H, *et al.* Recent progress on flexible lithium rechargeable batteries. *Energy Environ Sci*, 2014, 7: 538–551
  - 59 Wang X, Lu X, Liu B, *et al.* Flexible energy-storage devices: design consideration and recent progress. *Adv Mater*, 2014, 26: 4763–4782
  - 60 Hao C, Yang B, Wen F, *et al.* Flexible all-solid-state supercapacitors based on liquid-exfoliated black-phosphorus nanoflakes. *Adv Mater*, 2016, 28: 3194–3201
  - 61 Yang C, Ji X, Fan X, *et al.* Flexible aqueous Li-ion battery with high energy and power densities. *Adv Mater*, 2017, 29: 1701972
  - 62 Deng B, Lei T, Zhu W, *et al.* In-plane assembled orthorhombic  $\text{Nb}_2\text{O}_5$  nanorod films with high-rate  $\text{Li}^+$  intercalation for high-performance flexible li-ion capacitors. *Adv Funct Mater*, 2018, 28: 1704330
  - 63 Gui Q, Ba D, Zhao Z, *et al.* Synergistic coupling of ether electrolyte and 3D electrode enables titanates with extraordinary coulombic



efficiency and rate performance for sodium-ion capacitors. *Small Methods*, 2018, 3: 1800371

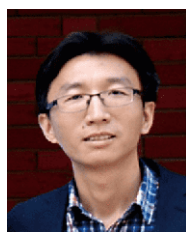
- 64 Zuo W, Li R, Zhou C, *et al.* Battery-supercapacitor hybrid devices: recent progress and future prospects. *Adv Sci*, 2017, 4: 1600539
- 65 Bard A J, Faulkner L R. *Electrochemical methods: Fundamentals and Applications*. New York: Jony Wiley & Sons, Inc., 2001
- 66 Funabiki A. Impedance study on the electrochemical lithium intercalation into natural graphite powder. *J Electrochem Soc*, 1998, 145: 172–178
- 67 Aurbach D. Common electroanalytical behavior of Li intercalation processes into graphite and transition metal oxides. *J Electrochem Soc*, 1998, 145: 3024–3034
- 68 Levi MD, Aurbach D. Simultaneous measurements and modeling of the electrochemical impedance and the cyclic voltammetric characteristics of graphite electrodes doped with lithium. *J Phys Chem B*, 1997, 101: 4630–4640
- 69 Macdonald J R. *Impedance Spectroscopy: Emphasizing Solid Materials and Systems*. New York: Jony Wiley & Sons, Inc., 1987
- 70 Chen Z, Augustyn V, Wen J, *et al.* High-performance supercapacitors based on intertwined CNT/V<sub>2</sub>O<sub>5</sub> nanowire nanocomposites. *Adv Mater*, 2011, 23: 791–795
- 71 Wang X, Li G, Chen Z, *et al.* High-performance supercapacitors based on nanocomposites of Nb<sub>2</sub>O<sub>5</sub> nanocrystals and carbon nanotubes. *Adv Energy Mater*, 2011, 1: 1089–1093
- 72 Lim E, Jo C, Kim H, *et al.* Facile synthesis of Nb<sub>2</sub>O<sub>5</sub>@carbon core-shell nanocrystals with controlled crystalline structure for high-power anodes in hybrid supercapacitors. *ACS Nano*, 2015, 9: 7497–7505
- 73 Song MY, Kim NR, Yoon HJ, *et al.* Long-lasting Nb<sub>2</sub>O<sub>5</sub>-based nanocomposite materials for Li-ion storage. *ACS Appl Mater Interfaces*, 2017, 9: 2267–2274
- 74 Wang Q, Wen Z, Li J. A hybrid supercapacitor fabricated with a carbon nanotube cathode and a TiO<sub>2</sub>-B nanowire anode. *Adv Funct Mater*, 2006, 16: 2141–2146
- 75 Jung HG, Venugopal N, Scrosati B, *et al.* A high energy and power density hybrid supercapacitor based on an advanced carbon-coated Li<sub>4</sub>Ti<sub>5</sub>O<sub>12</sub> electrode. *J Power Sources*, 2013, 221: 266–271
- 76 Yu D, Goh K, Wang H, *et al.* Scalable synthesis of hierarchically structured carbon nanotube-graphene fibres for capacitive energy storage. *Nat Nanotech*, 2014, 9: 555–562
- 77 Lu X, Yu M, Zhai T, *et al.* High energy density asymmetric quasi-solid-state supercapacitor based on porous vanadium nitride nanowire anode. *Nano Lett*, 2013, 13: 2628–2633
- 78 Xu J, Wang Q, Wang X, *et al.* Flexible asymmetric supercapacitors based upon Co<sub>9</sub>S<sub>8</sub> nanorod//Co<sub>3</sub>O<sub>4</sub>@RuO<sub>2</sub> nanosheet arrays on carbon cloth. *ACS Nano*, 2013, 7: 5453–5462
- 79 Kaempgen M, Chan CK, Ma J, *et al.* Printable thin film supercapacitors using single-walled carbon nanotubes. *Nano Lett*, 2009, 9: 1872–1876
- 80 El-Kady MF, Strong V, Dubin S, *et al.* Laser scribing of high-performance and flexible graphene-based electrochemical capacitors. *Science*, 2012, 335: 1326–1330

**Acknowledgements** This work was supported by the National Natural Science Foundation of China (51672205, 21673169 and 51972257), the National Key R&D Program of China (2016YFA0202602), and the Natural Science Foundation of Hubei Province (2018CFB581).

**Author contributions** Dong H and Lei T performed the experiments; Deng B wrote the paper with support from Liu J, Xiao L and Yue N. All authors contributed to the general discussion.

**Conflict of interest** The authors declare that they have no conflict of interest.

**Supplementary information** Supporting data are available in the online version of the paper.



**Jinping Liu** received his PhD degree from Central China Normal University (CCNU) in June 2009. During 2008–2011, he did visiting and post-doctoral research at Nanyang Technological University (NTU) in Singapore. He is currently Chair Professor at Wuhan University of Technology. The research interests of Dr. Liu's group include the synthesis of nanostructures and their electrochemical applications (batteries, supercapacitors and electrocatalysis).

## 退火调控的3D交联TiNb<sub>2</sub>O<sub>7</sub>纳米棒电极用于高效柔性锂离子电池

邓伯华<sup>1</sup>, 董浩洋<sup>1</sup>, 雷田雨<sup>1</sup>, 岳宁<sup>1</sup>, 肖亮<sup>1</sup>, 刘金平<sup>1,2\*</sup>

**摘要** TiNb<sub>2</sub>O<sub>7</sub>的理论比容量高达280 mA h g<sup>-1</sup>,是一类有前景的锂离子电池负极材料。然而其较差的电子导电性严重限制了其倍率性能的提升。在本文中,我们在柔性碳布表面直接生长3D交联的TiNb<sub>2</sub>O<sub>7</sub>纳米棒多孔负极,并将其首次应用于柔性锂离子电池;碳布的高导电性,单晶纳米棒结构较短的离子/电子传输路径以及良好的结构稳定性,有效提高了材料的倍率性能和循环稳定性。研究表明,TiNb<sub>2</sub>O<sub>7</sub>负极表现出优异的倍率性能(从1到40 C,容量保持率高达66.3%),出色的循环稳定性(>2000圈),以及良好的柔韧性(连续弯曲500次后容量无损失)。此外,将无粘结剂的TiNb<sub>2</sub>O<sub>7</sub>负极和商用活性炭正极搭配成锂离子电池,展现出了较高的质量和体积能量/功率密度(~100.6 W h kg<sup>-1</sup>/4108.8 W kg<sup>-1</sup>; 10.7 mW h cm<sup>-3</sup>/419.3 mW cm<sup>-3</sup>),优于先前报道的混合超级电容器,同时该器件可以在180°弯曲状态下为LED灯供电。